Climate Dynamics
https://doi.org/10.1007/s00382-021-06095-y

Recent Eurasian winter cooling partly caused by internal multidecadal variability amplified by Arctic sea ice-air interactions

Aiguo Dai[1] · **Jiechun Deng**[2]

Received: 13 August 2021 / Accepted: 2 December 2021

Abstract
Despite rapid global warming, Eurasia experienced unusual winter cooling from around 1992–2012, whose cause is still debated. By analyzing observations and model simulations, we show that the winter cooling from 1992 to 2012, as well as the enhanced winter warming from 1971–1991, over Eurasia partly resulted from internally-generated multidecadal variations related to variations in sea ice cover (SIC) and surface air temperature (Tas) over the Barents-Kara Seas (BKS). The BKS SIC and Tas variations concur with a multidecadal trend towards an anticyclonic (cyclonic) anomaly circulation over the Ural Mountains during 1992–2012 (1971–1991) that advected cold (warm) air from the Arctic (southwest Eurasia) into central Asia, contributing to the cooling (warming) over most Eurasia during 1992–2012 (1971–1991). These multidecadal variations in BKS SIC and Tas largely disappear, and the associated anomaly circulation and its influence on central Eurasia (CE) weaken when sea ice-air interactions are absent, although reduced multidecadal cooling over CE still exists in simulations without Arctic sea ice-air coupling. Because of the 10–20 day lifetime of Ural blocking, daily Arctic sea ice-air interactions, which are absent in all simulations with prescribed sea ice, are crucial for models to realistically simulate Ural blocking events and their decadal frequency and other changes that connect the BKS and CE Tas anomalies. BKS multidecadal warming is insufficient to induce CE cooling when Arctic sea ice-air interactions are turned off in our simulations. In contrast to the multidecadal BKS sea-ice decline, global-warming induced long-term sea-ice loss does not cause cooling over CE, likely due to other associated changes. As sea ice continues to melt away, its ability to cause such multidecadal variations and cooling over Eurasia will diminish.

Keywords Eurasian winter cooling · Arctic sea-ice loss · Barents-Kara Seas · Ural blocking · Global warming · Sea ice-air interactions

1 Introduction

Central Eurasia (CE) has experienced large winter cooling from about 1992–2012, in contrast to rapid warming over the Arctic and the rest of the world (Overland 2011; Cohen et al. 2014, 2020; Wallace et al. 2014; Johnson et al. 2018). Such cooling is unusual given that most of the world has been warming up rapidly in response to rising greenhouse gases (GHG) during the recent decades. Furthermore, the Eurasian cooling was linked to damaging extreme cold events over Eurasia during recent years (Liu et al. 2012; Wallace et al. 2014; Kug et al. 2015; Yao et al. 2017; Johnson et al. 2018). Thus, the cause of this unusual cooling has attracted considerable attention, yet it is still intensely debated (Kug et al 2015; Semenov and Latif 2015; Overland et al 2016; Huang et al 2017). Regression analyses linked the Eurasian cooling to warming over the Barents-Kara Seas (BKS; Outten and Esau 2012; Kug et al. 2015) through atmospheric anomaly circulation (Sorokina et al. 2016; Luo et al. 2016, 2017, 2018, 2019), but such results do not necessarily suggest a causal relationship, although the BKS is host to the largest and most significant sea-ice

✉ Aiguo Dai
adai@albany.edu

✉ Jiechun Deng
jcdeng@nuist.edu.cn

[1] Department of Atmospheric and Environmental Sciences, University at Albany, State University of New York, Albany, NY 12222, USA

[2] Key Laboratory of Meteorological Disaster, Ministry of Education, ILCEC, CIC-FEMD, Nanjing University of Information Science and Technology, Nanjing 210044, China

Published online: 04 January 2022

loss over the last four decades (Simmonds and Li 2021). Atmospheric modeling studies (Honda et al. 2009; Kug et al. 2015; Mori et al. 2014, 2019) using prescribed Arctic sea-ice cover and global sea surface temperatures (SSTs) suggest some weak cooling over CE in response to recent Arctic sea ice decline or diverse effects on CE (Zhang and Screen 2021); while other modeling studies (McCusker et al. 2016; Sun et al. 2016; Ogawa et al. 2018; Blackport et al. 2019; Koenigk et al. 2019; Dai and Song 2020) do not find such a connection between Arctic sea-ice loss and Eurasian cooling; instead, they suggest that the CE cooling likely resulted from internal variability, such as the interdecadal Pacific Oscillation (IPO; Deser et al. 2017; Matsumura and Kosaka 2019), although these modeling studies did not identify the specific source of the internal variability.

Furthermore, no future climate projections show any winter cooling or reduced warming over Eurasia as Arctic sea ice declines under increasing GHGs (Meehl et al. 2007; Collins et al. 2013; Lee et al. 2021), and coupled climate models do not underestimate the temperature link between BKS and CE (Screen and Blackport 2019). Recently, Dai and Song (2020) also did not find robust winter cooling over Eurasia either due to Arctic sea-ice loss and its associated Arctic amplification (AA) under GHG-induced warming or due to the GHG-induced background warming without AA. On the other hand, data analyses (Kug et al. 2015; Luo et al. 2016, 2017, 2018; Yao et al. 2017; Deser et al. 2017) suggest that the recent warming over BKS is accompanied by anticyclonic anomaly circulation or increased blocking over the Ural Mountains, which enhances cold advection into CE and causes cold anomalies there. Further, the recent BKS warming and sea-ice loss are linked to the Atlantic Multidecadal Oscillation (AMO) (Levitus et al. 2009; Day et al. 2012; Miles et al. 2014; Luo et al. 2017), although the recent AMO cycles may be partly forced by decadal changes in volcanic and anthropogenic aerosols (Qin et al. 2020a, b).

These findings contradict the claim (Mori et al. 2019) that GHG-induced sea-ice loss over BKS would lead to cold and more extreme winters over Eurasia, and they suggest that monotonic increases of GHGs cannot produce cooling over Eurasia even though it causes long-term Arctic sea-ice loss and enhanced Arctic warming. Instead, the recent Eurasian cooling may have resulted from (mainly internally-generated) multidecadal variations that are characterized by enhanced sea-ice loss, atmospheric warming and high pressure over BKS and increased cold advection into CE, leading to temporal multidecadal cooling over Eurasia. Here, we analyze observational and reanalysis data and novel model simulations to provide further evidence to support this hypothesis, examine the role of Arctic sea ice-air interactions, and discuss why previous modeling studies would produce contrasting results.

2 Data and model simulations

2.1 Observational and CMIP6 data

We used daily and monthly data for boreal winter (December-January–February or DJF) from 1950–2020 for sea surface temperature (SST), sea-ice concentration, surface air temperature (Tas), horizontal winds, and geopotential height fields from the newly released European Centre for Medium-Range Weather Forecasts (ECMWF) Reanalysis version 5 (ERA5) (Hersbach et al. 2020) on a 1° grid. We also analyzed the same data from 1950–2020 from the National Centers for Environmental Prediction (NCEP)/National Center for Atmospheric Research (NCAR) Reanalysis (NCEP/NCAR) (Kalnay et al. 1996) on a 2.5° grid. We used the Hadley Centre Global Sea Ice and Sea Surface Temperature dataset (HadISST) version 1.0 (Rayner et al. 2003) for SST and version 2.2 (Titchner and Rayner 2014) for sea-ice concentrations, and surface temperature data from the Hadley Centre/Climatic Research Unit Temperature dataset version 4 (HadCRUT4, Morice et al. 2012) and Goddard Institute for Space Studies (GISS) Surface Temperature (GISTEMP) Analysis version 4 (Lenssen et al. 2019) from National Aeronautics and Space Administration (NASA) for 1950–2020. These observational and reanalysis data are used in Figs. 1, 2 and Figs. S1–S6, which show similar results regarding BKS (40°–80°E, 70°–85°N) and CE (50°–120°E, 40°–60°N) Tas changes and the associated anomaly circulation patterns, although subtle differences exist among the different datasets. The BKS and CE regions were selected based on the Tas correlation patterns shown in Fig. S1.

We also used monthly data from four all-forcing historical (HIST) and future simulations from four CMIP6 (Eyring et al. 2016) models, namely, the CanESM5, CESM2-WACCM, IPSL-CM6A-LR, and MRI-ESM2-0 (other models did not have data up to year 2300 when we downloaded the data in 2020). The Shared Socioeconomic Pathways (SSP) 5–8.5 (SSP5-8.5) scenario was used, which corresponds to RCP8.5 of CMIP5 and represents a high emissions scenario. We analyzed the extended SSP5-8.5 simulations that ended in year 2300, when BKS winter sea ice melts away. Thus, these extended simulations allow us to investigate future Eurasian Tas variability when BKS has melted away. For the historical climate (1920–2019), all-forcing historical simulations (which ended in year 2014) were used for 1920–2014 and SSP5-8.5 simulations were used for 2015–2019; while SSP5-8.5 during 2200–2299 was used for the future climate. All the model outputs were remapped onto a 2.5° grid before analysis.

2.2 CESM1 simulations

The CESM1 model simulations used here are described in detail in Dai et al. (2019), Dai and Song (2020) and Deng and Dai (2021). The CESM1 (Hurrell et al. 2013) is a widely

used comprehensive earth system model that simulates the global, Arctic and midlatitude mean climate realistically. We ran the CESM1 with grid spacing of 2.5° longitude × ~2.0° latitude for the atmospheric model (using CAM4), and ~1.0° longitude × ~0.5° latitude for the sea-ice and ocean models.

In this study, we used the standard 500-year pre-industrial control run (CTL) with atmospheric CO_2 fixed at 284.7ppmv that has fully-coupled sea ice (i.e., with two-way sea ice-air interactions), and a second 500-year pre-industrial run (CTL_FixedIce) in which fixed daily sea ice cover (SIC) derived from the monthly climatology of the CTL run was used *only* in the coupler of the model north of 30°N for determining the fractional weights of the ice and water surfaces used to calculate the grid-box mean values of all surface exchange fluxes of energy, mass and momentum. We emphasize that in CTL_FixedIce sea ice was not fixed but allowed to evolve dynamically as in the standard CESM1, as the prescribed SIC was used only in the coupler and only for computing the ice and water surface fractions, but not inside the ice model. Thus, variations in internally-simulated SIC were not allowed to influence surface fluxes in CTL_FixedIce, but atmospheric and oceanic variations were allowed to affect surface fluxes and these flux variations were felt by sea ice. This effectively cut off the two-way sea ice-air interactions in CTL_FixedIce. The internal SIC variations in CTL_FixedIce were greatly reduced due to the dampened variations in surface fluxes as a result of the prescribed SIC in the flux calculations. Since we did not alter the flux calculations over ice and water surfaces, our use of the fixed SIC for calculating the ice and water fractional weights does not violate any physical laws, such as the conservation of energy and water. More information regarding this FixedIce setup is provided in Dai et al. (2019), Dai and Song (2020) and Deng and Dai (2021).

In addition, we also used a standard, fully coupled CESM1 235-year simulation with 1% per year increases in atmospheric CO_2 ($1\%CO_2$) and another 235-year $1\%CO_2$ run with Arctic sea ice treated as in CTL_FixedIce ($1\%CO_2$_FixedIce), in which internal sea ice variations and melting were greatly reduced and not felt by the atmosphere and ocean. We emphasize that the different responses to the CO_2 forcing (mainly in the Arctic) in the two $1\%CO_2$ simulations result from the lack of the sea ice-air coupling in $1\%CO_2$_FixedIce, and we removed the forced changes (including those in the Arctic) from our analyses. Thus, like the two CTL runs, the differences between the two $1\%CO_2$ simulations can be largely attributed to the impact of the sea ice-air interactions. The two $1\%CO_2$ runs are described and used in Dai et al. (2019) and Dai and Song (2020).

2.3 Analysis methods

2.3.1 Decadal-multidecadal variability

To quantify the internally-generated decadal-multidecadal variations, the externally-forced signal in all analyzed fields was first removed from both observations, reanalysis and model simulations following the method used previously (Dai et al. 2015; Qin et al. 2020a, b). Here we defined the forced signal as the time series of the area-mean surface air temperature (GMT) averaged over 60°S–75°N from the multi-model ensemble mean (MMM) of the 25 all-forcing historical runs from 25 CMIP6 models. For observations and reanalysis over 1950–2020 and historical simulations over 1920–2020, we used linear regression between the CMIP6 MMM GMT (as the x variable) and the given variable (e.g., Tas or sea-ice concentrations as the y variable) at each grid box to obtain the forced component in variable y. We then removed this forced component from variable y's original time series, so that the residual fields (referred to as the detrended fields) contain primarily unforced internal variability. This detrending procedure is a more effective way to remove most of the forced signal than the linear detrending method (Dai et al. 2015; Qin et al. 2020b). Similar procedure was applied to the CESM1 $1\%CO_2$ and $1\%CO_2$_FixedIce runs, except that their own GMT time series was used as the x variable in the linear regression; but for anomaly time series of BKS Tas and SIC, we used a 3rd-order polynomial fit in the detrending procedure (instead of the linear fit) to eliminate any nonlinear long-term trend, as BKS sea-ice concentrations decrease nonlinearly with increasing CO_2. For CMIP6 simulations under the SSP5-8.5 scenario during 2200–2299, the forced signal was simply removed using linear detrending, as BKS Tas and sea-ice concentrations become close to constant over this period. Please note that the detrending removes only the long-term trend, so that we can focus on multidecadal variations, which are irregular and noncyclic oscillations.

After removing the forced components, the internally-generated decadal-multidecadal variations were then obtained by applying a 9-year Lanczos low-pass filter with a 13-year half-response period. The linear trend of a given variable over a target segment (e.g., over a 21-year period as for 1992–2012) was calculated using the above filtered and detrended time series. For the model simulations, the linear trends over all 21-year moving segments were calculated for plotting their PDFs and for selecting the CE (or BKS) cooling and warming periods used to make the composite maps of the anomaly circulation. We required the trend to exceed the ± 1 standard deviation (SD) threshold, first selected the periods with the local strongest trend, and then selected those with the trends still outside the ± 1SD range but five years apart (this reduces the overlapping among the selected periods and allows more samples) from the nearest selected periods (see Fig. 4, S9-S10).

2.3.2 Statistical significance test

F-tests were used to test the significance of a change in the standard deviation of a given variable (data length = N) using the

effective degree of freedom defined as N/τ (where τ is the e-folding time scale over which the autocorrelation decays to $1/e$). Student's t-tests were applied to test whether multidecadal linear trends or correlations are statistically significant based on a 5% significance level. For a correlation between two strongly autocorrelated time series (X and Y of length N), the effective degree of freedom (N_e) was defined as: $N_e = N\left(1 + 2\sum_{i=1}^{10} X_i Y_i\right)^{-1}$, where X_i and Y_i indicate autocorrelations at i lags of the two series, respectively (Quenouille 1952).

2.3.3 AMO and atmospheric blocking

The AMO index was defined as the detrended DJF-mean SST anomalies (i.e., after removing externally-forced changes based on CMIP6 MMM following Qin et al. 2020b) averaged over the North Atlantic (0°–80°W, 0°–60°N). A bidimensional blocking index (Luo et al. 2015) was used to detect instantaneous atmospheric blocking over relatively high-latitudes based on the meridional gradients of daily 500-hPa geopotential height at each longitude:

$$GHGS_1(\lambda,\phi) = \frac{Z(\lambda,\phi) - Z\left(\lambda,\phi_S\right)}{\phi - \phi_S}$$

$$GHGS_2(\lambda,\phi) = \frac{Z\left(\lambda,\phi_S\right) - Z\left(\lambda,\phi_S - 15°\right)}{15°}$$

$$GHGN(\lambda,\phi) = \frac{Z\left(\lambda,\phi_N\right) - Z(\lambda,\phi)}{\phi_N - \phi}$$

where λ (ϕ) is the longitude (latitude) ranging from 0°–360° (30°–75°N) and ϕ_S=ϕ-15°, ϕ_N=ϕ+15°; and $Z(\lambda,\phi)$ is the daily 500-hPa geopotential height at a given grid point (λ,ϕ). $GHGS_1$ (GHGN) denotes the meridional gradients of geopotential height south (north) of the given grid point (λ,ϕ), and $GHGS_2$ is used to exclude low-latitude blocking and subtropical ridges over the Euro-Atlantic sector (Luo et al. 2015). Thus, an instantaneous blocking day was identified if a winter day satisfies the following criterion (Luo et al. 2015):

$GHGS_1(\lambda,\phi) > 0$

$GHGS_2(\lambda,\phi) < -5$ m per 1° latitude

$GHGN(\lambda,\phi) < -10$ m per 1° latitude

Accordingly, the atmospheric blocking frequency for each winter was defined as instantaneous blocking days expressed as a percentage of the winter days.

Because the temperature anomalies associated with blocking often extend from the surface to mid-troposphere (i.e., close to barotropic), it is common to use Z500 (instead of sea-level pressure) in the analysis of atmospheric blocking and pressure fields (e.g., Luo et al. 2016, 2018; Yao et al. 2017). Here, we follow this convention and use Z500 fields, plus low-level (i.e., 850 hPa) winds, to depict large-scale changes in atmospheric circulation.

Although our focus is on boreal winter, as the CE cooling is seen mostly in DJF, some atmospheric processes, such as those associated with the stratospheric polar vortex (Kim et al. 2014), may produce delayed effects on DJF Tas from autumn sea-ice variations. To the extent the ERA5, CESM1 and CMIP6 models are able to simulate these processes, such delayed effects should have already been included in the DJF variations examined here.

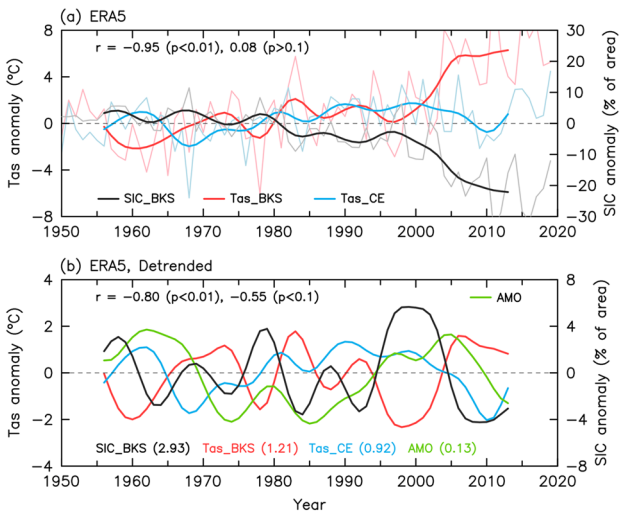

Fig. 1 Time series of surface air temperature and sea-ice concentrations from ERA5. (**a**) Anomaly time series of DJF-mean surface air temperature (Tas, left y axis) averaged over central Eurasia (CE, blue) and BKS (red) outlined in Fig. 2b, and BKS sea-ice concentration (SIC, black; right y axis) based on ERA5 reanalysis for 1950–2020. Light thin curves are for unsmoothed time series and thick curves are smoothed series using a 9-year Lanczos low-pass filtered with a 13-yr half-response period. (**b**) Same as (**a**) but with the forced signal removed and without the thin lines plus the similarly-filtered AMO index (green curve, multiplied by a factor of ten to use the left y axis) from ERA5. The forced signal at each grid box was removed before area-weighted averaging using a linear regression over 1950–2020 between the global (60°S–75°N) mean Tas (GMT) from CMIP6 multi-model ensemble mean (MMM) (as the x variable) and the local Tas or SIC from the reanalysis (as the y variable) (see Sect. 2.3). The correlation coefficients (r) and their p-values in **a**, **b** are, from left to right, between the smoothed BKS SIC and BKS Tas, and BKS Tas and CE Tas; and the respective correlations for detrended but unsmoothed time series are − 0.78 ($p<0.01$) and − 0.14 ($p>0.1$). The AMO and BKS SIC has a peak correlation of -0.31 ($p>0.1$) when AMO leads by ~13 years. The standard deviations (SD) of the smoothed and detrended time series in **b** are also given in parentheses with the same colors

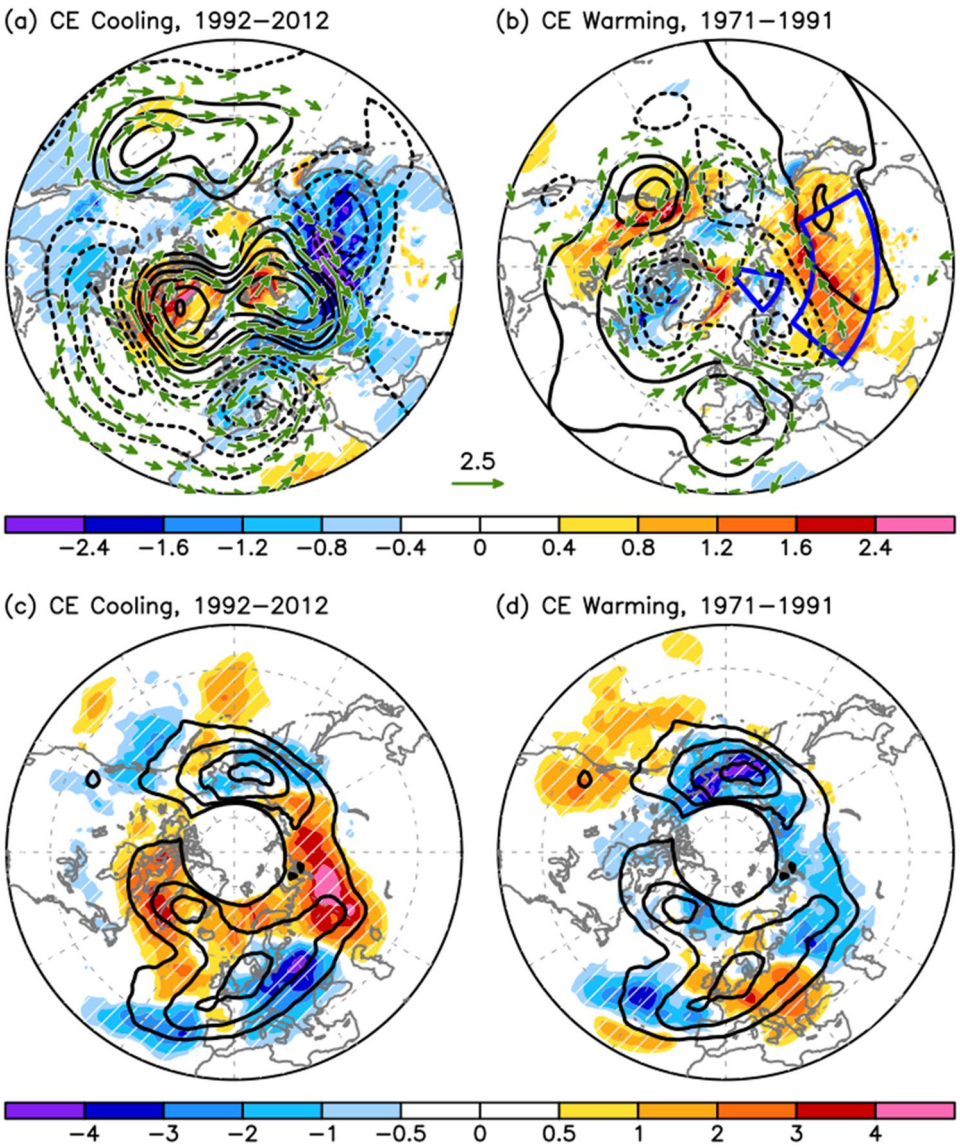

Fig. 2 Decadal trend maps of surface air temperature and atmospheric circulation fields from ERA5. (**a**, **b**) Linear trend maps over 20°–90°N of smoothed DJF-mean anomalies (after removing the forced signal, see Sect. 2.3) of Tas (color shading, in ℃ per decade), 850-hPa winds (vectors, in m s^{-1} per decade), and 500-hPa geopotential height (contours with an interval of 8, in gpm per decade; dashed contours are for negative values and the zero contour is omitted) from ERA5 for (**a**) the cooling period from 1992–2012 and (**b**) the warming period from 1971–1991. Only vectors with significant *u* or *v* component and larger than 0.8 m s^{-1} per decade are plotted. The outlined areas in **b** define the central Eurasian cooling region (50°–120°E, 40°–60°N) and the BKS (40°–80°E, 70°–85°N). (**c**, **d**) Linear trend maps over 30°–75°N of DJF-mean atmospheric blocking frequency (color shading, in % of winter days per decade) following Luo et al. (2015) based on ERA5 reanalysis for (**c**) 1992–2012 and (**d**) 1971–1991. Also shown (contours with an interval of 4%) is the 1961–1990 mean blocking frequency. The forced signal was removed in **c** and **d** similarly as in **a** and **b**, and a nine-point spatial smoothing was applied. The hatching in all panels indicates the trend of the shaded variable is statistically significant at the 5% level on the basis of a Student's *t*-test. The geopotential height trends (contours in **a**, **b**) over about 16 or below -16 gpm per decade are statistically significant

3 Results

3.1 Observational evidence of internally-generated Eurasian winter cooling

Observations and reanalysis data (Fig. 1 and Figs. S2-S4) show a rapid winter warming trend together with accelerated sea ice loss from around 1995–2016 over BKS, while winter Tas exhibits cooling over most Eurasia from about 1992–2012. The CE Tas started to increase again since ~ 2013 while BKS SIC continues to decrease or stays at a low level (Fig. 1a). These recent changes do not support the notion that BKS SIC loss causes CE cooling (Mori et al. 2014, 2019). After removing the externally-forced

changes associated with historical GHG and other forcing changes, the internally-generated decadal-multidecadal anomalies and their correlations among the BKS SIC, BKS Tas and CE Tas become clearer. The multidecadal variations reveal a warming trend from around 1971–1991 and then a cooling trend from around 1992–2012 in winter CE Tas, while it is approximately the opposite for winter BKS Tas (Figs. 1b, 2a-b and Figs. S2-S6). Because the multidecadal variations before and after the removal of the forced component are comparable, especially for CE Tas (Fig. 1a-b), we can conclude that the recent winter cooling trend over Eurasia from 1992–2012 likely resulted from internally-generated multidecadal variations, rather than a response to recent climate forcing or the GHG-induced sea-ice loss.

Associated with the recent warming over BKS, there exists a trend towards anticyclonic anomaly circulation from central Asia to Europe during 1992–2012, whose northeasterly winds advect cold and dry air from the Arctic into Eurasia, causing cooling over central Eurasia (Fig. 2a). The prevailing westerly winds over the region should advect this cooling eastward to cover most East Asia (Fig. 2a). In contrast, from 1971–1991 approximately the opposite anomaly circulation occurred from central Asia to Europe that advected warm and moist air from the southwest into central Eurasia, causing warming over most of midlatitude Asia (Fig. 2b). The cooling impact over Eurasia by an anticyclonic anomaly circulation has been reported previously (Kug et al. 2015; Luo et al. 2016, 2017, 2018, 2019; Yao et al. 2017). The circulation anomalies also appear to be responsible for the previously noticed Cold North America-Warm Arctic pattern during 1992–2012 (Overland et al. 2011; Cohen et al. 2014) and the opposite pattern during 1971–1991 (Fig. 2a–b and Fig. S6). The DJF-mean changes in temperature and pressure are associated with changes in sub-seasonal atmospheric blocking over the Ural Mountains region around 60°E, such as increased Ural blocking frequency during 1992–2012 (Fig. 2c and Fig. S6c) and changes in other aspects of the blocking (Luo et al. 2016, 2017, 2018; Yao et al. 2017). In contrast, the Ural blocking frequency decreased from 1971 to 1991 (Fig. 2d and Fig. S6d). Because the Ural blocking has a lifetime of 10–20 days (Luo et al. 2016, 2017), daily variations in BKS SIC and SST, which were missing in all previous atmospheric model simulations with specified SIC and SST, can be important for models to simulate atmospheric response (including Ural blocking) to Arctic changes. Missing the daily SIC variations, which is partially the case in our CTL_FixedIce run, would lead to reduced SIC and Tas variations over the BKS (Fig. 3) and weakened UB-like anomaly circulation that links CE Tas to BKS changes (Fig. 5), as shown below.

Thus, atmospheric circulation changes near the Ural Mountains associated with the BKS temperature anomalies lead to an anti-correlation of −0.55 ($p<0.1$) between BKS Tas and CE Tas on decadal-multidecadal time scales (Fig. 1b). Furthermore, the BKS SIC and Tas are negatively correlated ($r=-0.80$, $p<0.01$) on these time scales (Fig. 1b). These multidecadal variations are correlated with the AMO cycles with a time lag (e.g., $r=-0.31$ with $p>0.1$ between BKS SIC and AMO when AMO leads by ~ 13 years, Fig. 1b), as noticed previously (Levitus et al. 2009; Day et al. 2012; Miles et al. 2014; Luo et al. 2017). However, there also exist large anti-correlated decadal variations between BKS SIC and Tas (e.g., during the 1980s and 1990s) that are muted in the AMO index (Fig. 1b). This suggests that there may be additional processes besides the influence from North Atlantic SSTs (NASST) through incursion of warm Atlantic water during the recent AMO warm phase (Levitus et al. 2009; Day et al. 2012; Miles et al. 2014).

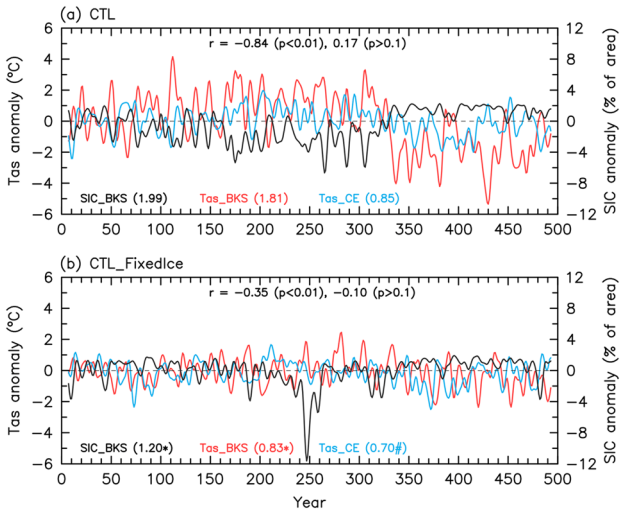

Fig. 3 Anomaly time series of surface air temperature and sea-ice concentrations from CESM1 control simulations. Time series of the smoothed anomalies of DJF-mean Tas (left *y* axis) averaged over central Eurasia (blue) and BKS (red), and BKS SIC (black; right *y* axis) from the CESM1 (**a**) CTL run and (**b**) CTL_FixedIce run during years 1–500. A 9-year Lanczos low-pass filter with a 13-year half-response period was applied to smooth the time series. The correlation coefficients (*r*) and their *p*-values in **a**, **b** are, from left to right, between BKS SIC and BKS Tas, and BKS Tas and CE Tas. The standard deviation (SD) of the time series is also given in parentheses with the same color, and the "*" ("#") indicates the SD difference between the CTL and CTL_FixedIce runs is statistically significant at the 5% (10%) level on the basis of a *F*-test. The BKS SIC in CTL_FixedIce unexpectedly dropped drastically during years 241–260 likely unrelated to the sea ice-air coupling, thus we excluded these years in SIC's SD calculation in panel b (including these years would increase the SD to 1.74)

3.2 Modeling evidence of the source of the multidecadal variability

Our model simulations show that the two-way sea ice-air interactions in the CTL run greatly increase the decadal-multidecadal variability in Tas (by 118% as measured by its standard deviation change) and SIC (by 66%) over the BKS compared with that in the CTL_FixedIce run (Fig. 3a-b), and over other sea-ice margin zones (Deng and Dai 2021). CE stands out as the only middle-latitude land area whose decadal-multidecadal variability is amplified significantly by the sea ice-air interactions (see Fig. 2 of Deng and Dai 2021). When we average the Tas and height trends over the 21-year periods selected based on the CE cooling or warming trends (Fig. 4), the composite anomaly circulation associated with CE cooling shows a high (low) pressure over BKS (CE) (Fig. Figure 5a), and the opposite circulation during CE warming periods (Fig. 5b). Such atmospheric anomaly circulation would lead to multidecadal cooling (Fig. 5a) or warming (Fig. 5b) over Eurasia through thermal advection, similar to recent observations (Fig. 2a–b) in spatial patterns but with smaller magnitudes. In fact, we found (Deng and Dai 2021) that multidecadal variability is greatly reduced not only in the Arctic (mainly over the BKS and other ice margin zones) but also in the North Atlantic (including the AMO) and CE when the sea ice-air interactions are cut off. We showed (Deng and Dai 2021) that sea ice-air interactions amplify SIC and Tas variations over the BKS and other ice margin zones mainly through local heat fluxes, and the multidecadal variations in NASSTs (i.e., AMO) and Atlantic Meridional Overturning Circulation (AMOC) mainly through changes in surface fluxes and ocean density in the subpolar North Atlantic, where North Atlantic deep water formation occurs. In other words, to a large degree, not only the multidecadal variability in BSK SIC and Tas, but also the AMO that was considered to be a major source of Arctic multidecadal variability (Levitus et al. 2009; Day et al. 2012; Miles et al. 2014; Luo et al. 2017) may have resulted, to a large extent, from sea ice-air interactions in the Arctic and subpolar North Atlantic.

The decadal-multidecadal variability in CE Tas increases by ~ 21% ($p = 0.09$) when the two-way sea ice-air interactions are turned on (Fig. 3), and the composite CE Tas cooling and warming trends are also enhanced significantly by ~ 31% ($p < 0.01$) and 22% ($p < 0.05$), respectively, along with large Tas and height differences over BKS between the two cases (Fig. 5). We notice that CE (and BKS) Tas decadal trends in CTL_FixedIce are noticeably reduced compared with CTL over certain periods (e.g., years 1–90, 130–170, and 340–500) but are comparable to CTL in other periods (e.g., years 90–130, 170–220, and 220–340) (Fig. 4). Multidecadal cooling and warming over CE still exist in the CTL_FixedIce run without Arctic two-way sea ice-air interactions, but they

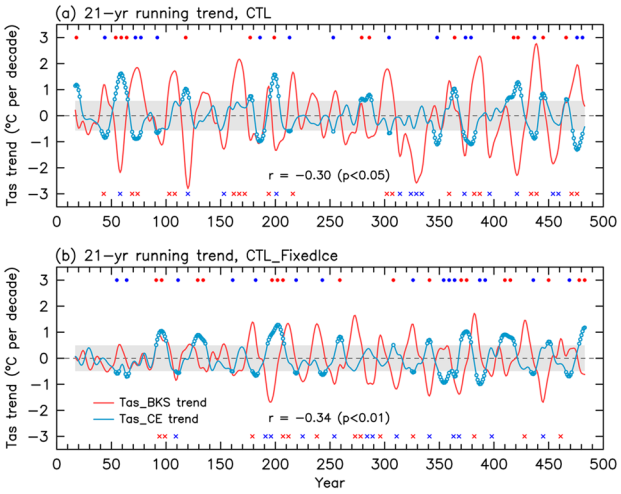

Fig. 4 Time series of 21-year running trends of the smoothed DJF-mean Tas anomalies averaged over CE (blue curve) and BKS (red curve) from the CESM1 (**a**) CTL run and (**b**) CTL_FixedIce run during years 1–500. The correlation coefficients (r) and their p-values between the blue and red curves are given on the panel. The gray shading denotes the ± 1 standard deviation (SD) range of the blue curve, and the blue open circles indicate the CE Tas trends outside this range. The blue and red dots (crosses) are the central years of the selected 21-year CE (BKS) cooling and warming periods (see Sect. 2.3), respectively, used to generate the composite trend maps shown in Figs. 5, 6

tend to occur with reduced intensity (Fig. 4) and northward-shifted and reduced area extent (Fig. 5a,c), as the associated BKS Tas and height trends weaken considerably (Fig. 5c-d). This suggests that there are other sources of variability (e.g., from the tropical Pacific and North Atlantic, Dai et al. 2015; Luo et al. 2021), besides the variability generated over the BKS, that can influence CE Tas decadal variations.

When we average the Tas and Z500 trends over the 21-year periods selected based on BKS warming or cooling trends (Fig. 4), the composite anomaly maps (Fig. 6) suggest the impacts from BKS on CE through the anomalous thermal advection. This differs from Fig. 5, which was derived by averaging over the selected CE cooling or warming periods that may not necessarily concur with BKS warming or cooling. Figure 6 shows that without the sea ice-air interactions, there is little decadal cooling over CE when decadal warming occurs over BKS (Fig. 6c). Noticeable cooling over CE would occur during BKS warming periods only when the sea ice-air coupling is turned on (Fig. 6a). To a less degree, this also applies to the BKS cooling case (Fig. 6b, d). Thus, Arctic sea ice-air interactions are necessary in order for BKS's decadal warming to induce significant decadal cooling over CE through thermal advection. This differs from Fig. 5, which suggests that Arctic sea ice-air coupling can enhance decadal trends over CE but such trends, albeit weakened, can still exist without the coupling.

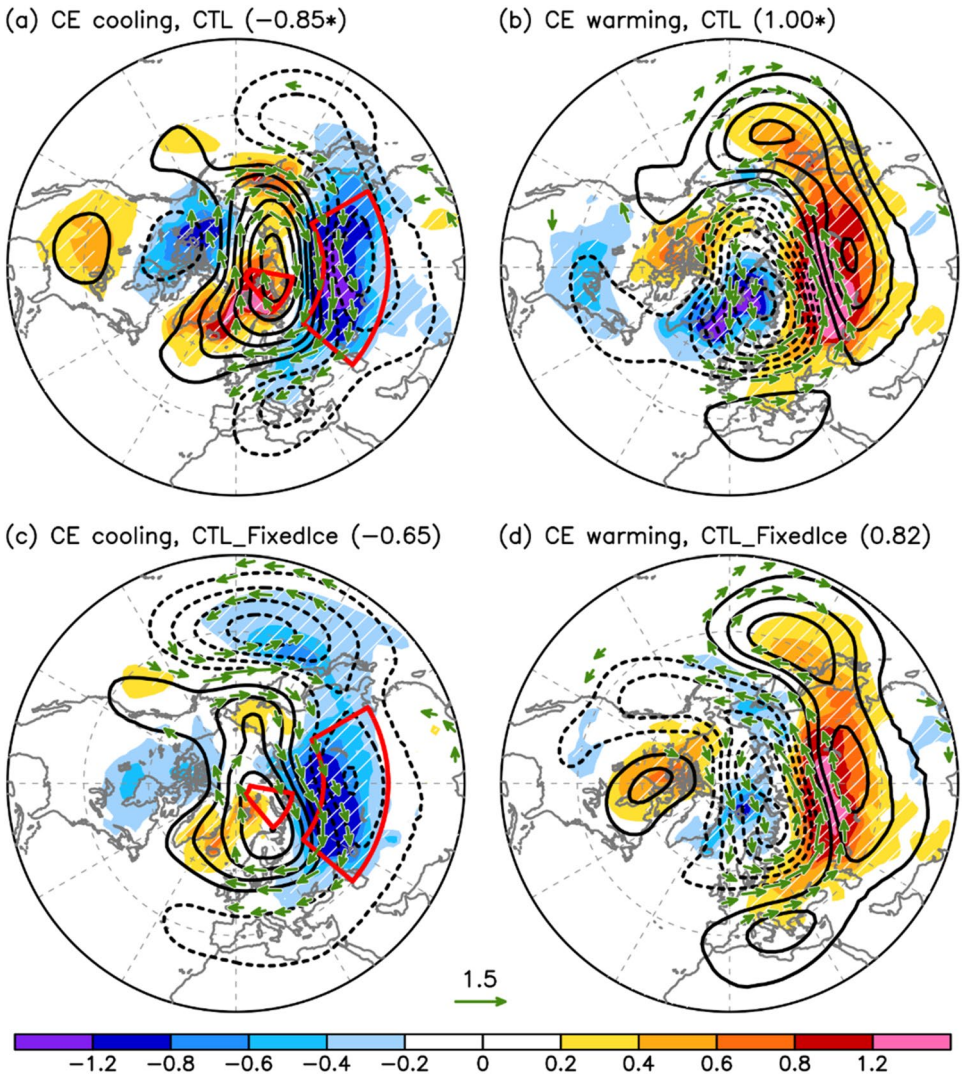

Fig. 5 Decadal trend maps of surface air temperature and atmospheric circulation fields from the CESM1 control simulations. (**a**, **b**) Linear trend maps over 20°–90°N of the smoothed DJF-mean anomalies of Tas (color shading, in ℃ per decade), 850-hPa winds (vectors, in m s^{-1} per decade), and 500-hPa geopotential height (contours with an interval of 4, in gpm per decade; dashed contours are for negative values and the zero contour is omitted) averaged over the selected Eurasian (**a**) cooling and (**b**) warming periods of 21 years from the CESM1 CTL run (see Sect. 2.3 and Fig. 4). (**c**, **d**) Same as (**a**, **b**), but from the CESM1 CTL_FixedIce run. The hatching and vectors (*u* or *v* component) indicate 70% of the selected periods show the same sign. Only vectors larger than 0.4 m s^{-1} per decade are plotted. All anomalies are relative to the mean of years 1–80. Note the smaller color and vector scales than in Fig. 2. The outlined areas in **a** and **c** are the BKS and CE regions as in Fig. 2b. The area-averaged CE Tas trend is also given in the parentheses on top of each panel, and the asterisk indicates the trend difference between the two cases is statistically significant at the 5% level on the basis of the Student's *t* test

The above results suggest that two-way sea ice-air interactions in BKS and other Arctic regions can not only greatly amplify the multidecadal variations in winter BKS Tas and SIC, but also noticeably enlarge the multidecadal variations in winter CE Tas. We also notice that the recent warming trend over CE from1971-1991 in ERA5 is within the 95th percentile of the trends over periods of similar length in the CESM1 CTL experiment (Fig. S7). While the CE cooling trend from 1992–2012 in ERA5 is outside the 5th percentile, it is still within the lower limit of the CTL distribution but outside the limit of CTL_FixedIce (Fig. S7). The standard deviation (SD) of the smoothed CE Tas anomalies in the CESM1 CTL run is 0.85 °C (Fig. 3a), which is about 8% smaller than that in ERA5 data (0.92 °C, Fig. 1b). The SD patterns of the smoothed Tas in the CESM1 CTL run are broadly comparable to those in ERA5, including an enhanced SD over CE (Deng and Dai 2021). Further, the correlation of the detrended and smoothed Tas between the BKS and CE during 1956–2013 in ERA5 (Fig. 1b) is not inconsistent with the distributions of the correlations over a

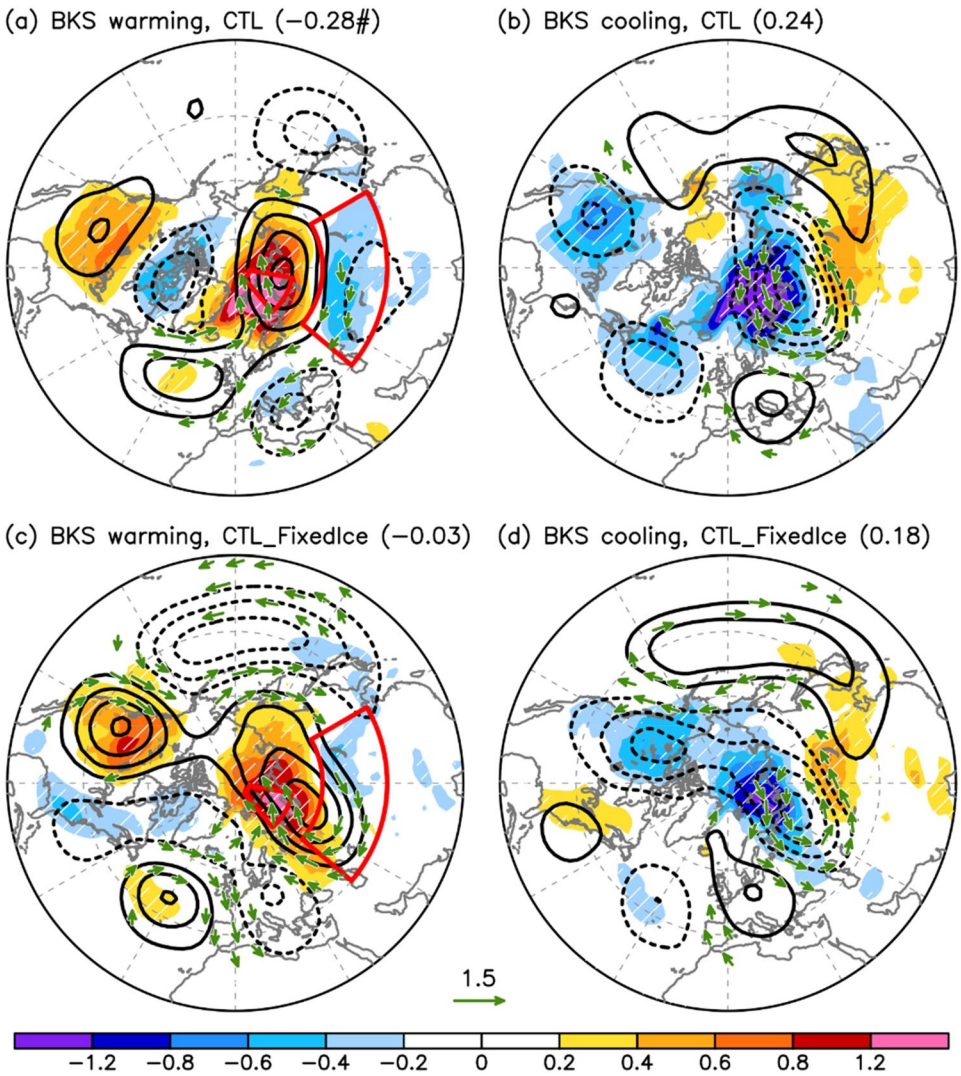

Fig. 6 Same as Fig. 5, but averaged over the selected BKS (**a**, **c**) warming and (**b**, **d**) cooling periods of 21 years from the CESM1 (**a**, **b**) CTL and (**c**, **d**) CTL_FixedIce runs during years 1–500. The "#" indicates the CE Tas trend difference between the two cases is statistically significant at the 10% level on the basis of the Student's *t* test

similar length of time periods in the fully-coupled CTL or 1%CO_2 runs (Fig. S8). The lack of the sea ice-interactions in these experiments reduces this consistency. These results suggest that the recent winter multidecadal warming from 1971–1991 and cooling from 1992–2012 over Eurasia may have partly resulted from the multidecadal variability over BKS generated or amplified by sea ice-air interactions. Without this sea ice-induced amplification, the influence from the AMO (Levitus et al. 2009; Day et al. 2012; Miles et al. 2014; Luo et al. 2017) and IPO (Deser et al. 2017; Matsumura and Kosaka 2019) on CE Tas would be reduced noticeably.

Winter sea ice over BKS will continue to exist and fluctuate under increasing CO_2 for the foreseeable future (Figs. 7, 8a-d), but eventually it would melt away if atmospheric CO_2 were to exceed six times the pre-industrial level (Figs. 7a, 11a) or in the twenty-third century under a high-emissions scenario (Fig. 8e–h). If that were to occur, decadal-multidecadal variations in BKS Tas would largely disappear, while the variations in CE Tas would also weaken in the CESM1 and three of the four CMIP6 models (Fig. 7a, 8e–h). Under FixedIce with the same 1%/year CO_2 increase, the internal decadal-multidecadal variability in BKS Tas and SIC is substantially reduced compared with the fully-coupled run, while the reduction in CE Tas's variability is relatively small (Fig. 7). Further, unlike the 1%CO_2 run, the variability for BKS Tas and SIC and CE Tas does not drop suddenly after about year 190 in the FixedIce run; in fact, it increases slightly as winter BKS SIC partially melts and becomes more variable over time (Figs. 7b,11b). These results further suggest a key role of the sea ice-air interactions for the variability over the BKS.

The internally-generated decadal-multidecadal variations superimposed on top of the CO_2-forced warming trend exhibit multidecadal cooling (Fig. 9a, c) or warming (Fig. 9b, d) and associated anomaly circulation over Eurasia that are unrelated to the monotonic CO_2 forcing and roughly resemble those in the pre-industrial control

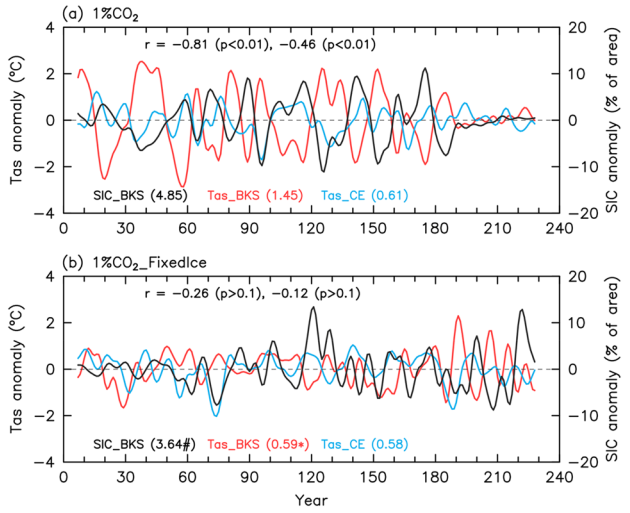

Fig. 7 Anomaly time series of surface air temperature and sea-ice concentrations from CESM1 1%CO_2 simulations. Time series of the smoothed DJF-mean Tas anomalies (left *y* axis; with the forced signal removed) averaged over central Eurasia (blue) and BKS (red), plus BKS SIC (black right *y* axis) from the CESM1 (**a**) 1%CO_2 run and (**b**) 1%CO_2_FixedIce run. The forced signal at each grid box was removed before area-weighted averaging using the linear regression between the global (60°S–75°N) mean Tas (GMT; as the *x* variable) and CE Tas (as the *y* variable) or using a 3rd-order polynomial fit for BKS Tas and SIC (as the *y* variable) (see Sect. 2.3). The correlation coefficients (*r*) and their *p*-values in **a**, **b** are, from left to right, between BKS SIC and BKS Tas, and BKS Tas and CE Tas during years 1–180. The standard deviation (SD) of the time series during years 1–180 is also given in parentheses with the same color, and the "*" ("#") indicates the SD difference between the CESM1 1%CO_2 and 1%CO_2_FixedIce runs is statistically significant at the 5% (10%) level on the basis of a *F* test

simulations (Fig. 5). The lack of the sea ice-air interactions in the 1%CO_2_FixedIce run not only eliminates the multidecadal Tas trends over BKS, but also reduces the CE cooling and warming trends by ~ 19% ($p = 0.14$) and 31% ($p = 0.04$), respectively, compared with the standard 1%CO_2 run, together with weakened anomaly circulation, a reduced cooling area and a northward-shifted cooling center (Fig. 9). The area and location changes of the Eurasian cooling may be related to the influences from the Pacific and North Atlantic, which also influence Eurasian Tas via changes in Ural blocking (Luo et al. 2021). These results under the 1%/year CO_2 increase are qualitatively consistent with the important role of the sea ice-air interactions in regulating the decadal-multidecadal variability over BKS and, to a lesser degree, over CE as revealed by the CTL experiments. Note that the mean climate is changing similarly under the same 1%/year CO_2 increase in these simulations, and the only difference is with or without the sea ice-air interactions and the associated Arctic change; thus, the differences between these two simulations can still be largely attributed to the effect of the sea ice-air interactions despite the changing mean climate, which was excluded in our analysis through detrending.

The multidecadal cooling and warming patterns and the associated anomaly circulation over Eurasia are also seen in the historical all-forcing simulations by other climate models (Fig. 10a-b). After sea ice in BKS and other Arctic regions melts away completely (Fig. 8e-h) and the sea ice-air interactions disappear in the twenty-third century, the multidecadal cooling and warming trends over CE and the associated anomaly circulation are reduced substantially (Fig. 10). Although in this case we cannot definitely attribute these differences to the lack of sea ice-air interactions because of the very different mean climates between those two periods, these results are at least consistent with our findings based on the CESM1 simulations.

3.3 Different effects of short-term and long-term sea-ice loss on CE Tas

Our analyses of the CESM1 standard and FixedIce 1%CO_2 experiments show (Fig. 11a-b) that warming (relative to CTL climatology) occurs over Eurasia in both experiments during all periods after year ~ 75, but weak cooling is seen during certain decades in the 1%CO_2-minus-FixedIce temperature difference for CE (Fig. 11c), which includes any effects from the large long-term sea-ice loss that existed in the 1%CO_2 run but was largely missing (before year ~ 130) in the FixedIce run. First, we do not see a long-term cooling trend in the CE Tas difference series (Fig. 11c), indicating that the larger sea-ice declining trend in the 1%CO_2 run does not cause a long-term cooling trend over CE. Second, the decadal-multidecadal fluctuations in the warming difference over CE cannot be explained by the *monotonic* CO_2 increase or *monotonic* sea-ice decrease; it must be related to the large fluctuations in CE Tas that are correlated with BKS Tas and SIC variations and result from internal variability, especially in the 1%CO_2 run (Fig. 7). These results suggest that GHG-induced long-term gradual sea-ice loss cannot produce persistent cooling over Eurasia, despite that internally-generated decadal large sea-ice loss may induce weak decadal cooling over Eurasia through enhanced cold advection. This finding is consistent with previous coupled modeling studies (e.g., Deser et al. 2016; Sun et al. 2018) that used the difference between a fully coupled simulation with projected future anthropogenic forcing and another simulation with the same forcing but with Arctic sea ice nudged to a fixed seasonal cycle of either present or future sea ice cover to isolate the effect sea ice loss on the climate, similar to our 1%CO_2-minus-FixedIce difference shown in Fig. 11c. These fully coupled simulations also did not show significant cooling over CE in response to future Arctic sea-ice loss, consistent with our Fig. 11c. We emphasize that although the two-way sea ice-air interactions are cut off in

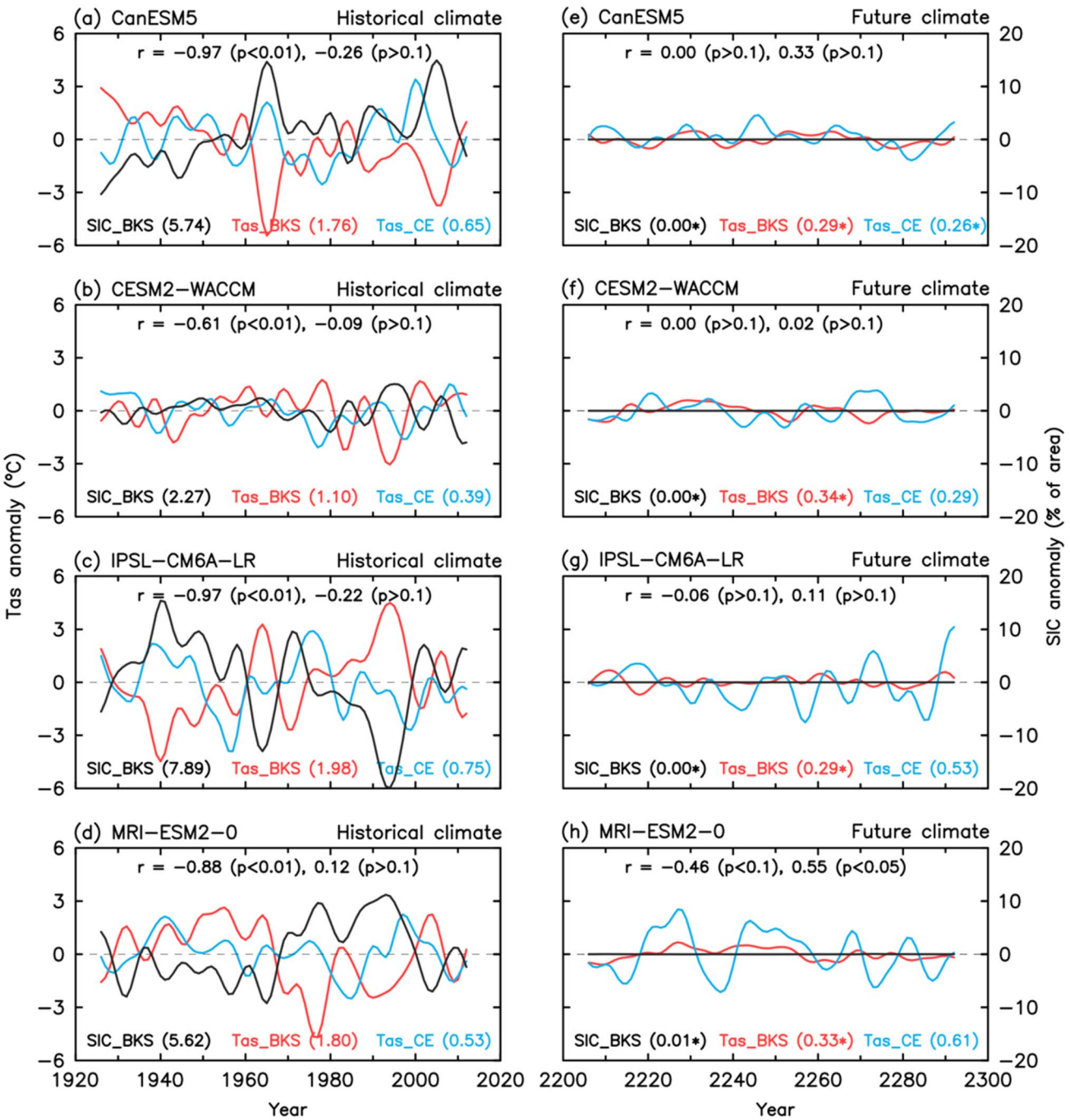

Fig. 8 Anomaly time series of surface air temperature and sea-ice concentrations from CMIP6 models. Time series of the smoothed DJF-mean Tas anomalies (left *y* axis; with the forced signal removed) averaged over central Eurasia (CE, blue; multiplied by a factor of two) and BKS (red), and BKS SIC (black; right *y* axis) during (**a**–**d**) 1920–2019 and (**e**–**h**) 2200–2299 based on one SSP5-8.5 simulation from four CMIP6 models: (**a**, **e**) CanESM5, (**b**, **f**) CESM2-WACCM, (**c**, **g**) IPSL-CM6A-LR, and (**d**, **h**) MRI-ESM2-0. For 1920–2019, the forced signal at each grid box was removed before area-weighted averaging using the linear regression over years 1920–2019 between the CMIP6 MMM global-mean Tas from 25 models (as the *x* variable) and the local Tas or SIC (as the *y* variable) from the given model; while for 2200–2299, the forced signal was removed using linear detrending of the averaged series over this period as BKS SIC and Tas become close to constant during this period. The correlation coefficients (*r*) and their *p*-values in the panels are, from left to right, between BKS SIC and BKS Tas, and BKS Tas and CE Tas. The standard deviation (SD) is also given in parentheses with the same color, and the asterisk indicates the SD difference between 1920–2019 and 2200–2299 is statistically significant at the 5% level on the basis of a *F* test

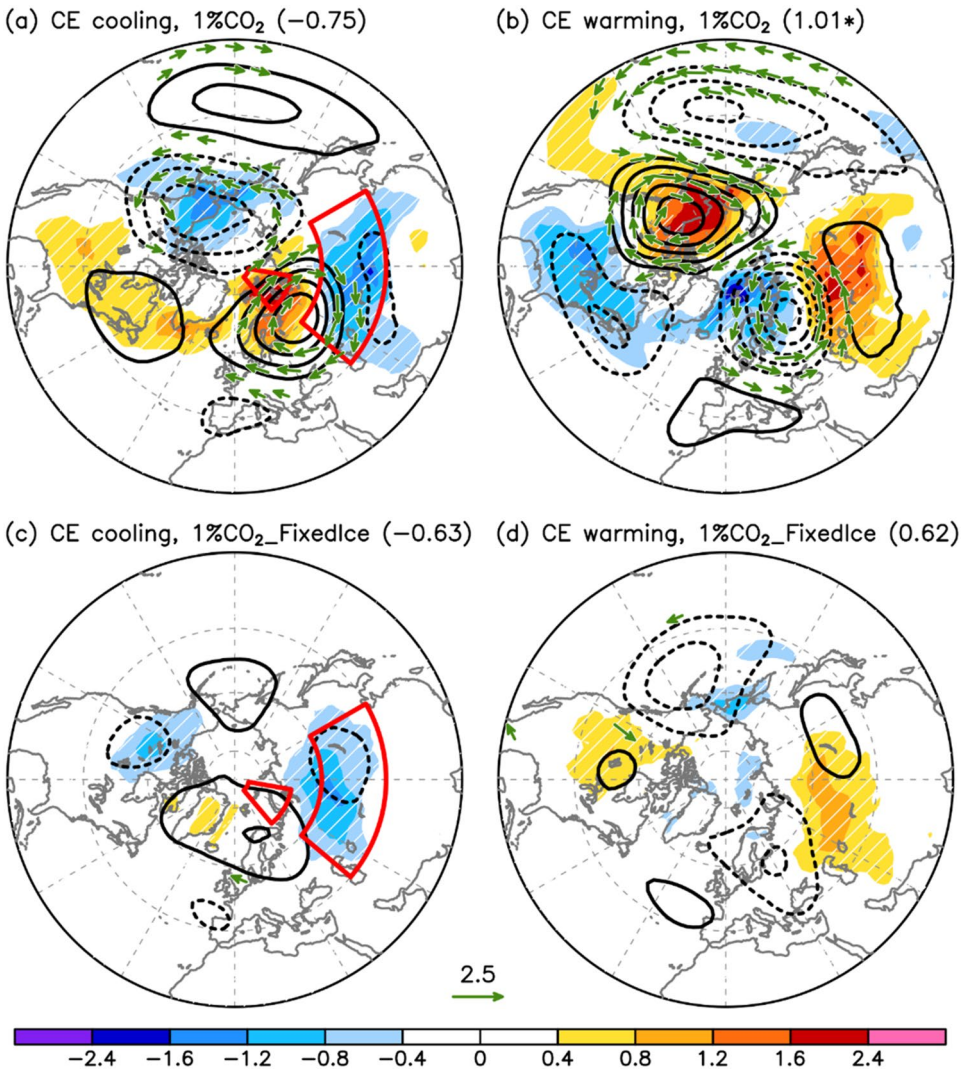

Fig. 9 Decadal trend maps of surface air temperature and atmospheric circulation anomaly fields from the CESM1 1%CO_2 simulations. (**a**, **b**) Linear trend maps over 20°–90°N of the smoothed DJF-mean anomalies (after removing the forced signal including forced changes in meridional temperature gradients) of Tas (color shading, in ℃ per decade), 850-hPa winds (vectors, in m s^{-1} per decade), and 500-hPa geopotential height (contours with an interval of 8, in gpm per decade; dashed contours are for negative values and the zero contour is omitted) averaged over the selected Eurasian (**a**) cooling and (**b**) warming periods of 21 years from years 1–180 of the CESM1 1%CO_2 run (see Sect. 2.3 and Fig. S9). (**c**, **d**) Same as (**a**, **b**), but from the CESM1 1%CO_2_FixedIce run. The hatching and vectors (*u* or *v* component) indicate 70% of the selected periods show the same sign. Only vectors larger than 0.8 m s^{-1} per decade are plotted. All anomalies are relative to the mean of years 1–80. Note the same color and vector scales as in Fig. 2a, b. The areas outlined by red lines in **a**, **c** are the BKS and CE regions as in Fig. 2b. The area-averaged CE Tas trend is also given in the parentheses on top of each panel, and the asterisk indicates the trend difference between the two cases is statistically significant at the 5% level on the basis of the Student's *t* test

our FixedIce run (and also likely in the previous nudged-ice runs, Deser et al. 2016; Sun et al. 2018), this should not greatly affect our simulated effect from the long-term sea-ice loss shown in Fig. 11c because this effect mainly comes from the fully coupled 1%CO_2 run as sea-ice loss in the FixedIce run is relatively small (before year ~ 130).

A major difference between the internally-generated decadal sea-ice decline and GHG-forced long-term sea-ice loss is that the GHG forcing also causes simultaneous warming, atmospheric circulation and other changes (e.g., reduced meridional temperature gradients that weaken thermal advection) over Eurasia that complicate the situation for the latter case. The magnitude of the BKS winter sea-ice loss caused by internal variability is also considerably larger than the GHG-induced sea-ice loss over the same length of time periods (Fig. 11), which makes the circulation anomaly more intense for the internally-generated changes (Figs. 2, 5). Although the accumulated winter BKS sea-ice loss over a long period (e.g.,

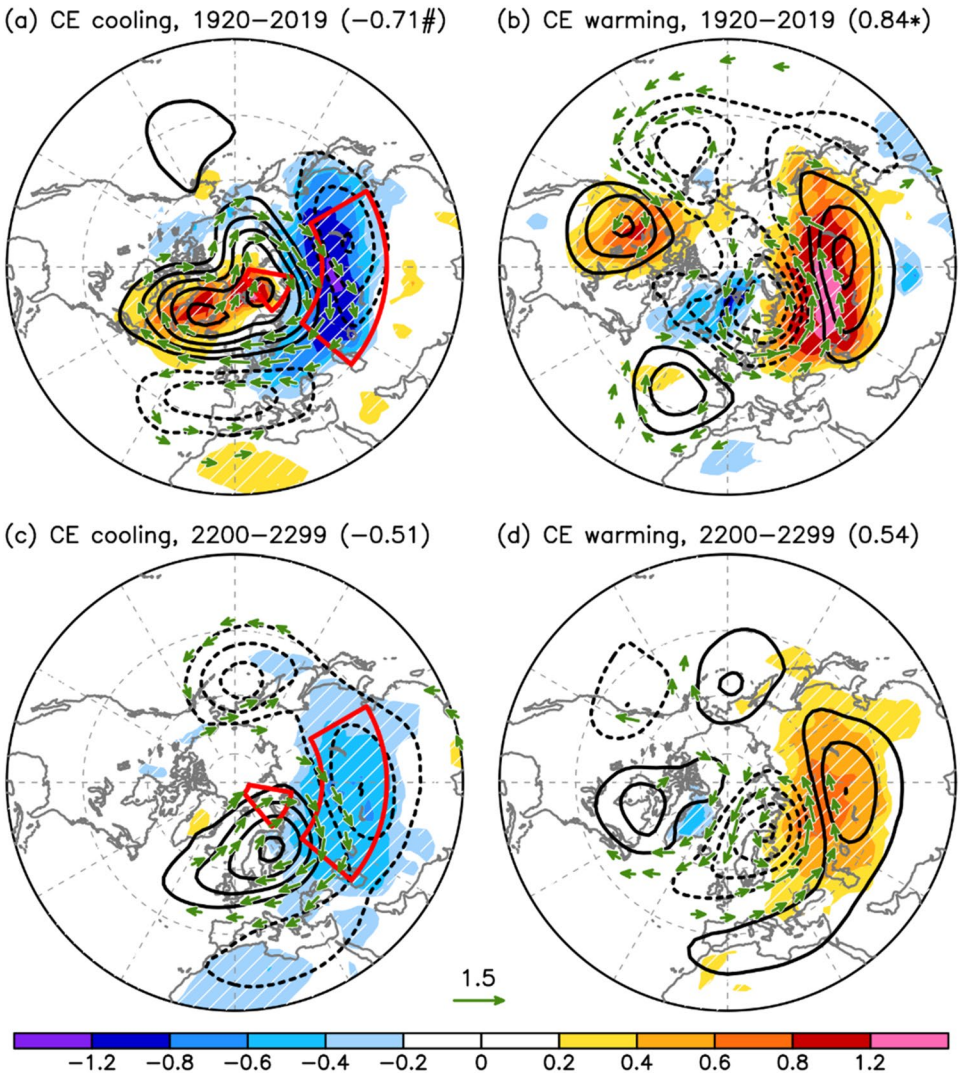

Fig. 10 Decadal trend maps of surface air temperature and atmospheric circulation fields from the CMIP6 models. (**a**, **b**) Linear trend maps over 20°–90°N of the smoothed DJF-mean anomalies (after removing the forced signal) of Tas (color shading, in ℃ per decade), 850-hPa winds (vectors, in m s^{-1} per decade), and 500-hPa geopotential height (contours with an interval of 4, in gpm per decade; dashed contours are for negative values and the zero contour is omitted) averaged over the selected Eurasian (**a**) cooling and (**b**) warming periods of 21 years based on one SSP5-8.5 simulation from each of the four CMIP6 models (see Sect. 2.3 and Fig. S10). The hatching and vectors (*u* or *v* component) indicate 70% of the selected periods shows the same sign. Only vectors larger than 0.4 m s^{-1} per decade are plotted. Note the smaller color and vector scales than in Fig. 2. The areas outlined by red lines in **a**, **c** are the BKS and CE regions as in Fig. 2b. The area-averaged CE Tas trend is also given in the parentheses on top of each panel, and the "*" ("#") indicates the trend difference between the two cases is statistically significant at the 5% (10%) level on the basis of the Student's *t* test

by the time of CO_2 quadrupling) can be large compared with the decadal variations (cf. Figs. 1, 11), by such time atmospheric circulation and other changes over Eurasia are more likely to be dominated by changes induced by the background global warming rather than BKS local warming and sea loss (Dai and Song 2020). These factors may contribute to the different impacts on Eurasian Tas from GHG-induced long-term sea-ice loss and internally-generated decadal sea-ice decline, but further investigation is needed to reveal the exact reasons (e.g., the role of reduced meridional temperature gradients and changes in Ural blocking) why the long-term sea ice loss would not cause a significant cooling over CE.

4 Summary and discussion

We have analyzed historical data from observations and ERA5 reanalysis from 1950–2020 and coupled model simulations using CESM1 and from CMIP6 to examine the causes of the recent winter cooling over central Eurasia (CE). Results show that, after removing externally-forced changes, surface air temperature (Tas) over the Barents-Kara Seas (BKS) and CE exhibits anticorrelated decadal-multidecadal variations caused by internal variability during 1950–2020. From 1992–2012, BKS experienced internally-generated multidecadal sea-ice decline and trends towards warming and high pressure, which produced anomalous anticyclonic circulation over the Ural Mountains (i.e., Ural blocking) that advected cold Arctic air into CE, causing cooling there. From ~ 1971–1991, roughly the opposite occurred over BKS and CE with anomalous cyclonic circulation advecting warm air from southwest Eurasia, causing warming over CE. Thus, both the winter cooling from 1992–2012 and the enhanced winter warming from 1971–1991 over Eurasia partly resulted from internally-generated multidecadal variations that are coupled to variations in sea ice cover (SIC) and Tas over BKS.

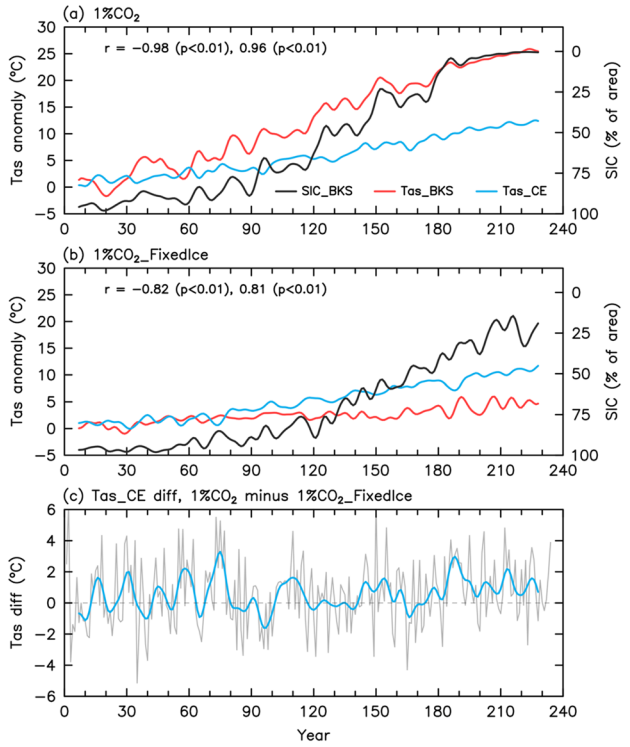

Fig. 11 Time series of DJF temperature over BKS and Central Eurasia and BKS sea-ice cover (SIC). Smoothed time series of DJF-mean surface air temperature (Tas) change (with the forced signal, relative the CTL climatology; left *y* axis, in °C) averaged over Central Eurasia (blue) and BKS (red), together with BKS SIC (black; right *y* axis, increases downward, in % of area) from the CESM1 (**a**) 1%CO_2 and (**b**) 1%CO_2_FixedIce run, and (**c**) their difference (blue line) in Central Eurasian Tas. A 9-yr low-pass filtering with a 13-yr half-response period was applied on all the curves (except the unsmoothed thin gray line in **c**) based on the Lanczos filter. The correlation coefficients (*r*) and their *p*-values in **a-b** are, from left to right, between BKS SIC and BKS Tas, and BKS Tas and CE Tas

Our modeling results further show that the multidecadal trends in BKS Tas, and CE Tas to a less degree, are amplified by the two-way sea ice-air interactions over BKS and other Arctic regions, as such trends would weaken substantially over BKS and noticeably for CE Tas when such interactions were cut off or when BKS sea ice melts away under GHG-induced warming in our CESM1 and other fully-coupled model simulations. Furthermore, Arctic sea ice-air interactions are necessary for BKS decadal warming to induce decadal cooling over CE through thermal advection, even though noticeable decadal cooling and warming trends over CE can still exist in model simulations without Arctic sea ice-air coupling. Because sea ice's amplification of surface warming occurs mainly in the cold season due to its large ocean-air temperature gradient (Dai et al. 2019) and also because atmospheric meridional temperature gradients and thus the effect of advection are strongest in winter (Dai and Deng 2021), the cooling effect over Eurasia from the anticyclonic circulation associated with BKS's warm anomalies is seen mainly in winter.

Our results are consistent with many previous studies (Kug et al. 2015; Luo et al. 2016, 2017, 2018; Yao et al. 2017; Deser et al. 2017) that showed a cooling effect over central Eurasia from anticyclonic anomaly circulation associated with BKS warm anomalies. They are also in agreement with many previous studies (Levitus et al. 2009; Day et al. 2012; Miles et al. 2014; Luo et al. 2017) that linked BKS sea-ice melting to recent AMO warm phase. However, these previous studies did not explicitly separate the externally-forced changes and internally-generated variations in historical data, and they also did not identify the specific source of the internal variability that might have contributed to the Eurasia cooling. In contrast, we further showed that the recent (1992–2012) cooling and previous (1971–1991) warming trends over Eurasia resulted from *internal* multidecadal variability that is amplified by two-way sea ice-air interactions in the Arctic, rather than due to long-term Arctic sea-ice loss caused by GHG-induced warming as suggested by some previous studies (e.g., Mori et al. 2019). While previous studies (e.g., Sorokina et al. 2016; Peings 2019; Blackport and Screen 2019; McGraw and Barnes 2020) suggested that the temperature variations over the BKS and central Eurasia are connected by atmospheric circulation, here we further showed that the blocking-like anomaly circulation connecting the two regions is enhanced by Arctic sea ice-air interactions.

In particular, the sea ice-air coupling on synoptic scales is important for Ural blocking events that have a lifetime of 10–20 days (Luo et al. 2016, 2017) and play a key role in connecting the BKS and CE temperature anomalies. Recent studies (e.g., Luo et al. 2016, 2017, 2019; Yao et al. 2017; Rudeva and Simmonds 2021) have emphasized the importance of synoptic-scale variability for Arctic-mid-latidude connections. Because of this, model simulations with prescribed or nudged Arctic sea-ice cover without or with reduced *daily* fluctuations (e.g., McCusker et al. 2016; Sun et al. 2016, 2018; Ogawa et al. 2018; Blackport et al. 2019; Koenigk et al. 2019; Ringgaard et al. 2020; Zhang and Screen 2021) will not be able to fully simulate Arctic sea ice-air coupling and Ural blocking on synoptic scales and thus will likely underestimate the connection between the BKS and CE, as shown by our CTL_FixedIce run. The albedo reduction method (Blackport and Kushner 2016) may allow sea ice-air interactions, but it does not work well for winter as the dominant process in Arctic winter is the insulation effect, not the albedo effect, of the ice layer. On the other hand, atmospheric model ensemble simulations (e.g., Mori et al. 2014, 2019) forced with climatological or observed monthly-mean SIC and SSTs may capture some of the anomaly circulation related to monthly-mean SIC and SST anomalies and thus the

resultant CE cooling shown in Fig. 5a, but the cooling magnitude in such experiments is much weaker than in observations (Mori et al. 2019; Screen and Blackport 2019). This is expected given the strong dampening effect from using fixed climatological SSTs (outside the Arctic) in their sea-ice only simulations (Mori et al. 2019). The use of observed monthly-mean SIC and SSTs (Sun et al. 2016; Ogawa et al. 2018) will allow the atmospheric model to capture some of the anomaly circulation, which may lead to a stronger cooling response over CE than in coupled simulations with reduced sea ice (Deser et al. 2016; Sun et al. 2018). In the latter case, SIC synoptic variability could be reduced due to nudging Arctic SIC to a fixed seasonal cycle (Sun et al. 2018). Thus, the lack of the two-way sea ice-air interactions on a daily basis in all these simulations (as in our FixedIce runs, because of the prescribed or nudged daily SIC interpolated from monthly-mean data), which are important for Ural blocking, would weaken the simulated circulation and temperature response over CE to sea-ice loss compared with fully coupled simulations. Furthermore, the observed recent sea-ice loss also includes internally-generated decadal-multidecadal variations that are not part of the response to historical GHG forcing. Thus, it is incorrect to use the CE Tas response to the observed sea-ice loss to infer the CE Tas response to future sea-ice loss caused by increasing GHGs (Mori et al. 2019).

Our results show that it is the internally-generated multidecadal fluctuations in BKS SIC and Tas, not GHG-induced long-term sea ice loss, that has likely contributed to the recent multidecadal cooling over Eurasia. This finding is consistent with the fact that no future climate projections (Meehl et al. 2009; Collins et al. 2013) show any winter cooling or reduced warming over central Eurasia, but contradicts the claim (Mori et al. 2019) that the weak cooling effect over central Eurasia from recent BKS sea-ice loss seen in atmospheric models represents an impact from the GHG-induced long-term Arctic sea-ice decline and that such impact over Eurasia would strengthen as Arctic sea-ice loss continues (which is not supported by the changes since ~ 2013, Fig. 1a). To the contrary, we found that the influence from BKS on Eurasian Tas will weaken as BKS sea ice melts away and the ice-air interactions diminish over BKS and other Arctic regions. However, further investigation is needed on the exact reasons why the GHG-induced long-term BKS sea-ice loss would not cause cooling over central Eurasia through anomaly cold advection, in contrast to what is seen for multidecadal variations.

Supplementary Information The online version contains supplementary material available at https://doi.org/10.1007/s00382-021-06095-y.

Acknowledgements J.D. was supported by the National Natural Science Foundation of China (grant nos. 42088101 and 41705054). A.D. was supported by the National Science Foundation (grant nos. AGS-2015780 and OISE-1743738).

Author contributions AD formulated the main ideas, contributed to the design of the analyses and figures, wrote the first draft of the paper, and designed the CESM1 simulations and made all the CESM1 simulations except CTL_FixedIce, which was ran by JD. JD contributed to the main ideas, did all the analyses, made all the figures, and helped writing the manuscript.

Funding This work was funded by NSF (grants nos. AGS-2015780 and OISE-1743738), and the National Natural Science Foundation of China (grant nos. 42088101 and 41705054).

Data availability All observational data used in this study are publicly available and can be downloaded from the corresponding websites (The ERA5 reanalysis: https://cds.climate.copernicus.eu/cdsapp#!/search?type=dataset; The NCEP/NCAR reanalysis: https://psl.noaa.gov/data/gridded/data.ncep.reanalysis.html; HadISST: https://www.metoffice.gov.uk/hadobs/; HadCRUT4: http://hadobs.metoffice.com/hadcrut4/; GISTEMP4: https://data.giss.nasa.gov/gistemp/). The CMIP6 outputs used in this study can be obtained from https://esgf-node.llnl.gov/projects/esgf-llnl/. The CESM1 model data used in this study are available from the authors upon request.

Code availability The CESM1 model code is available from https://www.cesm.ucar.edu/models/cesm1.2/.

Declarations

Conflict of interest None.

References

Blackport R, Kushner PJ (2016) The transient and equilibrium climate response to rapid summertime sea ice loss in CCSM4. J Clim 29:401–417. https://doi.org/10.1175/JCLI-D-15-0284.1

Blackport R, Screen JA (2019) Influence of Arctic sea ice loss in autumn compared to that in winter on the atmospheric circulation. Geophys Res Lett 46:2213–2221. https://doi.org/10.1029/2018GL081469

Blackport R, Screen J, van der Wiel K, Bintanja R (2019) Minimal influence of reduced Arctic sea ice on coincident cold winters in mid-latitudes. Nat Clim Change 9:697–704. https://doi.org/10.1038/s41558-019-0551-4

Cohen J, Screen JA, Furtado JC et al (2014) Recent arctic amplification and extreme mid-latitude weather. Nat Geosci 7:627–637. https://doi.org/10.1038/ngeo2234

Cohen J, Zhang X, Francis J et al (2020) Divergent consensuses on arctic amplification influence on midlatitude severe winter weather. Nat Clim Change 10:20–29. https://doi.org/10.1038/s41558-019-0662-y

Collins MR et al. (2013) Long-term climate change: projections, commitments and irreversibility. In: climate change: the physical science basis. Contribution of Working Group I to the Fifth Assessment Report of the Intergovernmental Panel on Climate Change. In: Stocker TF, Qin D, Plattner G-K, Tignor M, Allen

SK, Boschung J, Nauels A, Xia Y., Bex V, Midgley PM (eds.) Cambridge University Press, Cambridge

Dai A, Deng J (2021) Arctic amplification weakens the variability of daily temperatures over northern mid-to-high latitudes. J Clim 34:2591–2609. https://doi.org/10.1175/JCLI-D-20-0514.1

Dai A, Song M (2020) Little influence of Arctic amplification on mid-latitude climate. Nat Clim Change 10:231–237. https://doi.org/10.1038/s41558-020-0694-3

Dai A, Fyfe JC, Xie S-P, Dai X (2015) Decadal modulation of global surface temperature by internal climate variability. Nature Clim Change 5:555–559. https://doi.org/10.1038/nclimate2605

Dai A, Luo D, Song M, Liu J (2019) Arctic amplification is caused by sea-ice loss under increasing CO_2. Nat Commun 10:121. https://doi.org/10.1038/s41467-018-07954-9

Day JJ, Hargreaves JC, Annan JD, Abe-Ouchi A (2012) Sources of multidecadal variability in Arctic sea ice extent. Environ Res Lett 7:034011. https://doi.org/10.1088/1748-9326/7/3/034011

Deng J, Dai A (2021) Sea ice-air interactions amplify multidecadal variability in the North Atlantic and Arctic region. Nat Comm., under review. (Preprint available from http://www.atmos.albany.edu/facstaff/adai/paper/Deng-Dai-Arctic-DecadalVar-NComm-1stSub.pdf)

Deser C, Sun L, Tomas RA, Screen J (2016) Does ocean coupling matter for the northern extratropical response to projected Arctic sea ice loss? Geophys Res Lett 43:2149–2157. https://doi.org/10.1002/2016GL067792

Deser C, Guo R, Lehner F (2017) The relative contributions of tropical pacific sea surface temperatures and atmospheric internal variability to the recent global warming hiatus. Geophys Res Lett 44:7945–7954. https://doi.org/10.1002/2017GL074273

Eyring V, Bony S, Meehl GA et al (2016) Overview of the coupled model intercomparison project phase 6 (CMIP6) experimental design and organization. Geosci Model Dev 9:1937–1958. https://doi.org/10.5194/gmd-9-1937-2016

Hersbach H, Bell B, Berrisford P et al (2020) The ERA5 global reanalysis. Q J Roy Met Soc 146:1999–2049. https://doi.org/10.1002/qj.3803

Honda M, Inoue J, Yamane S (2009) Influence of low arctic sea-ice minima on anomalously cold Eurasian winters. Geophys Res Lett 36:L08707. https://doi.org/10.1029/2008GL037079

Huang J, Xie Y, Guan X et al (2017) The dynamics of the warming hiatus over the Northern Hemisphere. Clim Dyn 48:429–446. https://doi.org/10.1007/s00382-016-3085-8

Hurrell JW, Holland MM, Gent PR et al (2013) The community earth system model: a framework for collaborative research. Bull Am Meteorol Soc 94:1339–1360. https://doi.org/10.1175/BAMS-D-12-00121.1

Johnson NC, Xie SP, Kosaka Y, Li X (2018) Increasing occurrence of cold and warm extremes during the recent global warming slowdown. Nat Commun 9:1724. https://doi.org/10.1038/s41467-018-04040-y

Kalnay E, Kanamitsu M, Kistler R et al (1996) The NCEP/NCAR 40-year reanalysis project. Bull Amer Meteor Soc 77:437–472. https://doi.org/10.1175/1520-0477(1996)077%3c0437:TNYRP%3e2.0.CO;2

Kim BM, Son SW, Min SK et al (2014) Weakening of the stratospheric polar vortex by Arctic sea-ice loss. Nat Commun 5:4646. https://doi.org/10.1038/ncomms5646

Koenigk T, Gao Y, Gastineau G et al (2019) Impact of Arctic sea ice variations on winter temperature anomalies in northern hemispheric land areas. Clim Dyn 52:3111–3137. https://doi.org/10.1007/s00382-018-4305-1

Kug J-S, Jeong J-H, Jang Y-S et al (2015) Two distinct influences of arctic warming on cold winters over North America and East Asia. Nat Geosci 8:759–762. https://doi.org/10.1038/ngeo2517

Lee J-Y, Marotzke J, Bala G, Cao L, and Coauthors (2021) Future global climate: Scenario-based projections and near-term information. Climate Change 2021: The Physical Science Basis. Contribution of Working Group I to the Sixth Assessment Report of the Intergovernmental Panel on Climate Change. In: Masson-Delmotte V, et al. (eds.), Cambridge University Press, Cambridge

Lenssen N, Schmidt GA, Hansen JE et al (2019) Improvements in the GISTEMP uncertainty model. J Geophys Res Atmos 124:6307–6326. https://doi.org/10.1029/2018JD029522

Levitus S, Matishov G, Seidov D, Smolyar I (2009) Barents Sea multidecadal variability. Geophys Res Lett 36:L19604. https://doi.org/10.1029/2009GL039847

Liu J, Curry JA, Wang H, Song M, Horton RM (2012) Impact of declining Arctic sea ice on winter snowfall. Proc Natl Acad Sci USA 109:4074–4079. https://doi.org/10.1073/pnas.1114910109

Luo D, Yao Y, Dai A (2015) Decadal relationship between European blocking and the North atlantic oscillation during 1978–2011. Part I: atlantic conditions. J Atmos Sci 72:1152–1173. https://doi.org/10.1175/JAS-D-14-0039.1

Luo D, Xiao Y, Yao Y et al (2016) Impact of Ural blocking on winter warm Arctic-cold Eurasian anomalies. Part i: blocking-induced amplification. J Clim 29:3925–3947. https://doi.org/10.1175/JCLI-D-15-0611.1

Luo D, Chen Y, Dai A et al (2017) Winter Eurasian cooling linked with the Atlantic multidecadal oscillation. Environ Res Lett 12:125002. https://doi.org/10.1088/1748-9326/aa8de8

Luo D, Chen X, Dai A, Simmonds I (2018) Changes in atmospheric blocking circulations linked with winter Arctic sea-ice loss: a new perspective. J Clim 31:7661–7678. https://doi.org/10.1175/JCLI-D-18-0040.1

Luo D, Chen X, Overland J, Simmonds I, Wu Y, Zhang P (2019) Weakened potential vorticity barrier linked to recent winter Arctic sea ice loss and midlatitude cold extremes. J Climate 32:4235–4261

Luo B, Luo D, Dai A, Simmonds I, Wu L (2021) The modulation of Interdecadal Pacific Oscillation and Atlantic Multidecadal Oscillation on winter Eurasian cold anomaly via the Ural blocking change. Clim Dyn. https://doi.org/10.21203/rs.3.rs-437125/v1

Matsumura S, Kosaka Y (2019) Arctic-Eurasian climate linkage induced by tropical ocean variability. Nat Commun 10:3441. https://doi.org/10.1038/s41467-019-11359-7

McCusker KE, Fyfe JC, Sigmond M (2016) Twenty-five winters of unexpected Eurasian cooling unlikely due to arctic sea ice loss. Nat Geosci 9:838–842. https://doi.org/10.1038/ngeo2820

McGraw MC, Barnes EA (2020) New insights on subseasonal arctic–midlatitude causal connections from a regularized regression model. J Climate 33:213–228. https://doi.org/10.1175/JCLI-D-19-0142.1

Meehl GA, et al. (2007) Global climate projections. In: climate change 2007: the physical science basis. contribution of working group I to the fourth assessment report of the intergovernmental panel on climate change. In: Solomon S, Qin D, Manning M, Chen Z, Marquis M, Averyt KB, Tignor M, Miller KL (eds). Cambridge University Press, Cambridge

Miles MW, Divine DV, Furevik T et al (2014) A signal of persistent Atlantic multidecadal variability in Arctic sea ice *Geophys*. Res Lett 41:463–469. https://doi.org/10.1002/2013GL058084

Mori M, Watanabe M, Shiogama H et al (2014) Robust Arctic sea-ice influence on the frequent Eurasian cold winters in past decades. Nat Geosci 7:869–873. https://doi.org/10.1038/ngeo2277

Mori M, Kosaka Y, Watanabe M et al (2019) A reconciled estimate of the influence of Arctic sea-ice loss on recent Eurasian cooling. Nat Clim Change 9:123–129. https://doi.org/10.1038/s41558-018-0379-3

Morice CP, Kennedy JJ, Rayner NA et al (2012) Quantifying uncertainties in global and regional temperature change using an ensemble

of observational estimates: the HadCRUT4 dataset. J Geophys Res 117:D08101. https://doi.org/10.1029/2011JD017187

Ogawa F, Keenlyside N, Gao Y et al (2018) Evaluating impacts of recent Arctic sea ice loss on the northern hemisphere winter climate change. Geophys Res Lett 45:3255–3263. https://doi.org/10.1002/2017GL076502

Outten S, Esau I (2012) A link between Arctic sea ice and recent cooling trends over Eurasia. Clim Change 110:1069–1075. https://doi.org/10.1007/s10584-011-0334-z

Overland JE, Wood KR, Wang M (2011) Warm Arctic—Cold continents: climate impacts of the newly open Arctic Sea. Polar Res 30:15787. https://doi.org/10.3402/polar.v30i0.15787

Overland JE, Dethloff K, Francis JA et al (2016) Nonlinear response of mid-latitude weather to the changing Arctic. Nat Clim Change 6:992–998. https://doi.org/10.1038/nclimate3121

Peings Y (2019) Ural blocking as a driver of early-winter stratospheric warmings. Geophys Res Lett 46:5460–5468. https://doi.org/10.1029/2019GL082097

Qin M, Dai A, Hua W (2020a) Aerosol-forced multi-decadal variations across all ocean basins in models and observations since. Sci Adv 6:0425. https://doi.org/10.1126/sciadv.abb0425

Qin M, Dai A, Hua W (2020b) Quantifying contributions of internal variability and external forcing to Atlantic multidecadal variability since. Geophys Res Lett 1:e2020GL089504. https://doi.org/10.1029/2020GL089504

Quenouille MH (1952) Associated Measurements, 242. Butterworths Scientific Publications, London and Academic Press, New York

Rayner NA, Parker DE, Horton EB et al (2003) Global analyses of sea surface temperature, sea ice, and night marine air temperature since the late nineteenth century. J Geophys Res 108:4407. https://doi.org/10.1029/2002JD002670

Ringgaard IM, Yang S, Kaas E et al (2020) Barents-Kara sea ice and European winters in EC-Earth. Clim Dyn 54:3323–3338. https://doi.org/10.1007/s00382-020-05174-w

Rudeva I, Simmonds I (2021) Midlatitude winter extreme temperature events and connections with anomalies in the Arctic and tropics. J Climate 34:3733–3749

Screen JA, Blackport R (2019) Is sea-ice-driven Eurasian cooling too weak in models? Nat Clim Change 9:934–946. https://doi.org/10.1038/s41558-019-0635-1

Semenov VA, Latif M (2015) Nonlinear winter atmospheric circulation response to Arctic sea ice concentration anomalies for different periods during 1966–2012. Environ Res Lett 10:054020. https://doi.org/10.1088/1748-9326/10/5/054020

Simmonds I, Li M (2021) Trends and variability in polar sea ice, global atmospheric circulations, and baroclinicity. Ann NY Acad Sci. https://doi.org/10.1111/nyas.14673

Sorokina SA, Li C, Wettstein JJ, Kvamstø NG (2016) Observed atmospheric coupling between Barents Sea ice and the Warm-Arctic Cold-Siberian anomaly pattern. J Climate 29:495–511. https://doi.org/10.1175/JCLI-D-15-0046.1

Sun L, Perlwitz J, Hoerling M (2016) What caused the recent "warm Arctic, cold continents" trend pattern in winter temperatures? Geophys Res Lett 43:5345–5352. https://doi.org/10.1002/2016GL069024

Sun L, Alexander M, Deser C (2018) Evolution of the global coupled climate response to Arctic sea ice loss during 1990–2090 and its contribution to climate change. J Climate 31:7823–7843. https://doi.org/10.1175/JCLI-D-18-0134.1

Titchner HA, Rayner NA (2014) The met office hadley centre sea ice and sea surface temperature data set, version 2: 1. Sea ice concentrations. J Geophys Res Atmos 119:2864–2889. https://doi.org/10.1002/2013JD020316

Wallace JM, Held IM, Thompson D et al (2014) Global warming and winter weather. Science 343:729–730. https://doi.org/10.1126/science.343.6172.729

Yao Y, Luo D, Dai A, Simmonds I (2017) Increased quasi-stationarity and persistence of Ural blocking and Eurasian extreme cold events in response to Arctic warming. Part I: insights from observational analyses. J Clim 30:3549–3568. https://doi.org/10.1175/JCLI-D-16-0261.1

Zhang R, Screen JA (2021) Diverse Eurasian winter temperature responses to Barents-Kara sea ice anomalies of different magnitudes and seasonality. Geophys Res Lett 48:e2021GL092726. https://doi.org/10.1029/2021GL092726